Taoming Liu
Department of Electrical Engineering
and Computer Science,
Case Western Reserve University,
Cleveland, OH 44106
e-mail: txl168@case.edu

Nate Lombard Poirot
Department of Mechanical and
Aerospace Engineering,
Case Western Reserve University,
Cleveland, OH 44106
e-mail: njl49@case.edu

Tipakorn Greigarn
Department of Electrical Engineering
and Computer Science,
Case Western Reserve University,
Cleveland, OH 44106
e-mail: txg92@case.edu

M. Cenk Çavuşoğlu
Department of Electrical Engineering
and Computer Science,
Case Western Reserve University,
Cleveland, OH 44106
e-mail: mcc14@case.edu

Design of a Magnetic Resonance Imaging Guided Magnetically Actuated Steerable Catheter

This paper presents design optimization of a magnetic resonance imaging (MRI) actuated steerable catheter for atrial fibrillation ablation in the left atrium. The catheter prototype, built over polymer tubing, is embedded with current-carrying electromagnetic coils. The prototype can be deflected to a desired location by controlling the currents passing through the coils. The design objective is to develop a prototype that can successfully accomplish the ablation task. To complete the tasks, the catheter needs to be capable of reaching a set of desired targets selected by a physician on the chamber and keeping a stable contact with the chamber surface. The design process is based on the maximization of the steering performance of the catheter by evaluating its workspace in free space. The selected design is validated by performing a simulation of an ablation intervention on a virtual model of the left atrium with a real atrium geometry. This validation shows that the prototype can reach every target required by the ablation intervention and provide an appropriate contact force against the chamber. [DOI: 10.1115/1.4036095]

1 Introduction

Catheter ablation is a minimally invasive technique used for the treatment of atrial fibrillation [1,2]. In Fig. 1(*a*), a catheter passes through the femoral vein and the right atrium, and penetrates into the left atrium by passing through the atrial septum. The catheter is guided to access the area of pulmonary vein ostia and create circumferential lesions around the ostia by using radiofrequency energy. The lesions create barriers that prevent spread of irregular electrical signals causing the cardiac arrhythmia.

Magnetic resonance imaging (MRI) has been proven to be indispensable to the improvement of the catheter ablation procedure due to its superior soft-tissue visualization with no radiation exposure [3]. In catheter ablation, MRI has been used both preprocedurally to gather a detailed anatomical information of the left atrium and related areas, and postprocedurally to detect complications and visualize lesions [4]. Real-time catheter guidance and lesion visualization using MRI has also been demonstrated [3,4].

Robotic catheters have emerged as a promising alternative in catheter ablation. Some of the advantages include less physical demand on the physician, lower radiation exposure, greater catheter stability, and higher reproducibility. The MRI-actuated catheters were proposed in Refs. [5] and [6]. A general concept of an MRI-actuated steerable catheter is shown in Fig. 1(*b*). The catheter built over polymer tubing is embedded with a set of current-carrying coils. The catheter is then deflected by passing currents through the coils which generate magnetic torques under the MRI scanner's magnetic field. The currents can be controlled from the control room to remotely steer the catheter. Thus, with MRI-actuated catheters, mapping, remote-steering, ablation guidance, and lesion visualization can all be performed in the MRI environment. Gudino et al. [6], Liu and Cavusoglu [7], and Liu et al. [8] have successfully demonstrated the three-dimensional deflection of the MRI-actuated catheter inside a clinical MRI scanner.

This paper focuses on the optimization of the MRI-actuated steerable catheter design with structure shown in Fig. 1(*b*), so as to optimally perform left atrial ablation intervention. The catheter design optimization discussed in this paper refers to the design of the distal segment of a regular clinical catheter that will be located inside the left atrium (Fig. 1(*a*)). The remaining proximal segment of the catheter body is subject to a different set of design criteria. For example, proximal part of the catheter body would need to provide structural strength and stiffness to facilitate insertion of the catheter instead of providing flexibility for dexterous steering. Design of proximal segments of the catheter is well studied and is not specific to the proposed MRI guided catheter actuation scheme, and as such, is not considered in this paper.

The goal of this intervention is to create one circular lesion around each ostia of the pulmonary vein in the left atrium. Successful ablation intervention requires the catheter to have sufficient workspace to reach the ablation targets and to generate sufficient contact forces to maintain a stable contact with the tissue. A stable contact with enough contact force (CF) is critical to create lesions with appropriate depths for improving success rate of the intervention and reducing the recurrence rate.

The design of the prototype includes two subproblems: material selection of the catheter and design optimization of the coil actuators (including construction and placement). A three-dimensional (3D) model of an MRI-actuated catheter was proposed and validated by Liu et al. [7,8]. This model indicates that the deflection of catheter is related to mechanical properties of the construction material for the catheter, such as Young's modulus, Poisson's ratio, shear modulus and density. Therefore, the factorial design experiment method [9] is used for the material selection to investigate the effects of these properties on the performance. The catheter design also requires the selection of the actuator parameters. Each coil set on the catheter is composed of a set of three coils (one axial and two side coils) as shown in Fig. 1(*b*). The number

Manuscript received June 24, 2016; final manuscript received February 25, 2017; published online May 3, 2017. Assoc. Editor: Marc Horner.

of windings and the effective areas for each coil, as well as the location of the coil sets on the catheter, need to be determined to optimize the performance of the catheter system.

In this study, the catheter material selection and the actuator parameter selection are performed sequentially to reduce the computational complexity of the optimization. The reachable workspace of the catheter, as quantified by the range of deflection angles that can be achieved by the catheter design, is used as the metric of performance in the design optimization.

The final design of the prototype is validated in a simulation of left atrial fibrillation ablation intervention by evaluating the reachability of the catheter tip to the desired targets and the achievable contact force using a realistic model of the heart.

The remainder of the paper is organized as follows: Previous studies are discussed in Sec. 2. Section 3 reviews the deflection model of the catheter under external loads. Section 4 presents the process of choosing an appropriate material for the catheter. Section 5 presents optimization of the electromagnetic coil parameters and selection of the locations for the coils. A demonstration of the performance of the catheter is presented in Sec. 6, followed by the conclusions presented in Sec. 7.

2 Related Studies

Fu et al. [10] summarized the types of the active catheters employing different actuation methods in the previous literature. Magnetic actuation is one of the promising and emerging actuation methods employed. One advantage of magnetic actuation is the ability to place the actuation on the tip rather than at the proximal end outside patient body, thus increasing the bandwidth by reducing backlash and friction.

Muller et al. [11] reviewed different actuation methods in the literature for catheter navigation under MRI guidance. The general approach involves using an external magnetic field to produce magnetic torques or forces on the catheter tip by employing electromagnetic microcoils [5–7,12–15], ferromagnetic or magnetized materials [16–18] or even permanent magnets [19,20].

The design of a remotely steerable catheter is typically evaluated based on its steering performance and its adaptability to anatomical constraints in its clinical task. The steering performance is characterized in Ref. [11] as bending angles of the catheter tip, time to achieve bending, degree of rotation and miniaturization capacity of the design. Gosselin et al. [17] quantified the deflections of the catheter when the distance separating two ferromagnetic spheres are changed, and also measured magnetic forces generated by gradient changes. Settecase et al. [13] measured deflection angles of the catheter when winding turns of solenoids on 1.8Fr and 5Fr catheters were changed under 1.5 T and 3 T MRI scanners. Losey et al. [14] demonstrated a magnetically assisted remote-controlled (MARC) catheter for endovascular navigation under real-time MR imaging guidance. But like Refs. [13] and [17], this MARC catheter [14] was only investigated for the steering motion of the catheter on a plane. Recently, Moftakhar et al. [15] developed the third-generation MARC catheter, which can deflect in multiple planes.

In atrial fibrillation ablation, contact force between the catheter tip and the tissue has been noted to be an important factor for the outcome of the procedure [21,22]. An ablation intervention with a contact force of less than 10 g (100 mN) was indicated to have a higher recurrence rate than the one with a contact force of more than 10 g [22].

To the best of our knowledge, there are no earlier studies in the literature which discussed the MRI-actuated catheter design based on task and anatomical constraints. In terms of catheter-sized continuum robots, there are several earlier studies on the design optimization of concentric tube robots [23–25] based on anatomical and surgical task constraints.

3 Catheter Deflection Model

Modeling the proposed MRI-actuated catheter's three-dimensional deflection motion in free space, including bending and torsion was developed in Refs. [8] and [26]. In the proposed kinematic model, the catheter is approximated to be composed of a set of finite segments (shown in Fig. 2). The deflection of an individual segment is solved using beam theory and the Bernoulli–Euler law [8,26]. Then the force/torque equilibrium equations for each of the segments are then setup based on each segment's deflection angles.

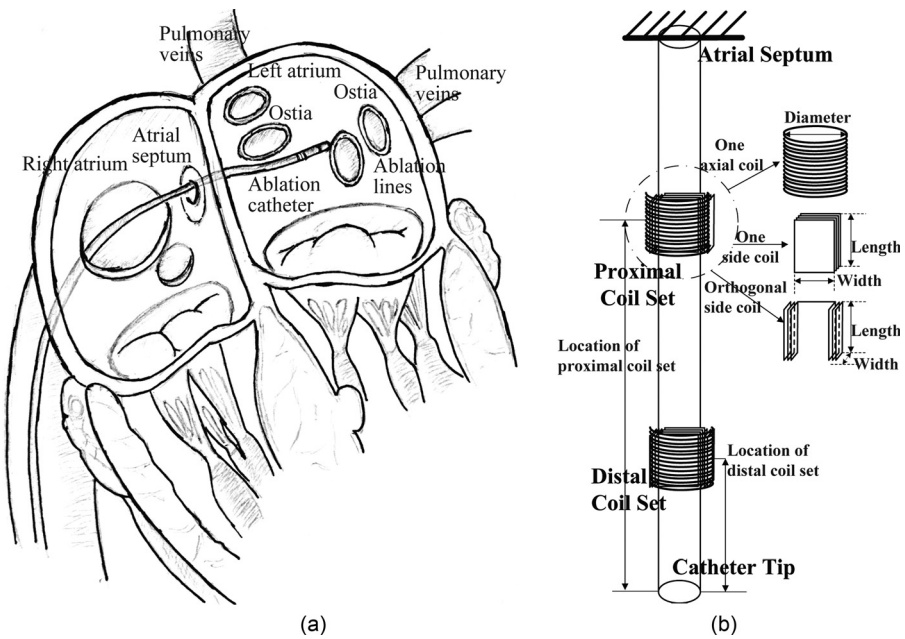

Fig. 1 (*a*) An illustration of left atrial fibrillation ablation in the left atrium. (Copyright IEEE 2014. Reprinted with permission [7].) (*b*) A general structure of an MRI-actuated steerable catheter. The catheter is embedded with two coil sets (proximal coil set and distal coil set). Each coil set includes one axial coil and two orthogonal side coil.

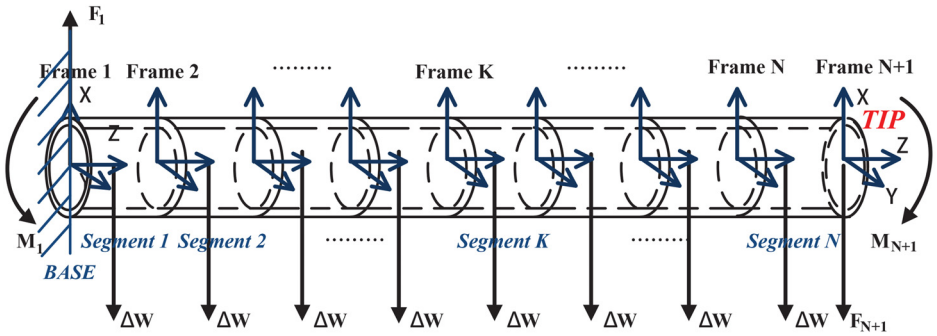

Fig. 2 Diagram of a catheter equipped with one set of embedded current-carrying coils, which is divided into *N* finite segments. (Copyright IEEE 2014. Reprinted with permission [7].)

The equilibrium equations for each segment ($i \in \{1, \ldots, N\}$) are presented in the below equation,

$$M_i = R_{i,i+1}M_{i+1} + P_{i,i+1} \times (R_{i,i+1}F_i) + Q_{i,i+1} \times (R_{i,1}\triangle W_i) \quad (1)$$

where the M_i and F_i represent the torque and force vectors acting on the ith segment, vector ΔW_i represents the weight of the ith segment, $P_{i,i+1}$ and $Q_{i,i+1}$ represent the end point and the center of the ith segment in frame i coordinates, and $R_{i,i+1}$ represents the rotation matrix between two ends on the ith segment. Here, F_{N+1} and M_{N+1} are, respectively, the external force and moment acting on the tip of the catheter. The resulting deflection of each segment ($i \in \{1, \ldots, N\}$) is then given by

$$S_i \cdot M_i = C_i \cdot X_i \quad (2)$$

where X_i represents the vector of deflection and torsion angles of the ith segment, S_i represents a matrix including the area moments of inertia and the area product of inertia of the ith segment cross section, C_i represents the stiffness matrix of the ith segment considering the material properties (such as Young's modulus and shear modulus). The specific details of the deflection model are explained in Refs. [8] and [26].

The magnetic torque from the electromagnetic coils embedded on the catheter can be computed by the cross product of magnetic moment and magnetic field. For example, if electromagnetic coils are embedded on the kth link, additional magnetic torque M_k given by

$$M_k = \boldsymbol{\mu}_k \times (R_{k,1}B_0) \quad (3)$$

is added to the kth link equation in Eq. (1), where the vector B_0 represents the main magnetic field of the MRI system relative to the base frame and the $\boldsymbol{\mu}_k$ represents the total magnetization vector of the catheter coils relative to frame k.

When catheter is being used for ablation, the catheter in contact with surface is under the combined loads of the magnetic torques from these coils, the contact force exerted back from the tissue, possibly friction force on the contacting surface, and the weights of the catheter and the coils (Fig. 3). In order to model the catheter deflections during contact, the model in Refs. [8] and [26] has been slightly modified by incorporating the contact forces applied on the catheter tip in the equilibrium equation of the last segment. Thus, mathematically, the external force F_{N+1} is calculated as

$$F_{N+1} = F_{con} + F_{fric} \quad (4)$$

by including the contact force, F_{con}, and the friction force, F_{fric}.

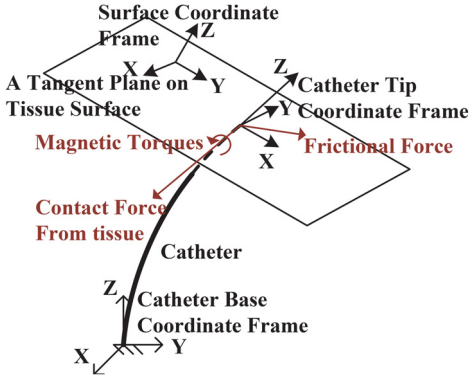

Fig. 3 Illustration of a catheter in point-contact with a chamber surface on a tangent plane

4 Selection of Catheter Material

A typical ablation catheter may have different mechanical characteristics at different parts of its shaft to satisfy different design requirements. As such, different parts of the catheter may be constructed from different materials. The focus of the paper is to design the distal segment of the catheter inside the left atrium (Fig. 1(*a*)). The key requirement for this segment is to be flexible so as to allow the catheter to be steerable enough for atrial fibrillation ablation. The chosen material also needs to be biocompatible. This section focuses on the effects of different materials on the steering performance.

4.1 Factorial Design for Material Selection. The steering performance of the catheter is related to three mechanical properties of the material: Young's modulus, Poisson's ratio, and density. Young's modulus characterizes the stiffness of an elastic isotropic material. Poisson's ratio gives the relationship between the transverse and axial strains of a material. The density of the material determines the weight of the prototype given its dimensions.

For completeness of coverage of catheter material, common biocompatible materials, which are specified in literature for construction of catheters, such as in some patents [27–29], are summarized in Table 1.[1] There are various types of catheters, such as urinary catheters, intravascular catheters, gastrointestinal catheters, angiographic catheters, and microcatheters for neurovascular and ophthalmic interventions. All these types of catheters serve a broad range of distinct functions and thus they have varying levels of stiffness values depending on their applications. It is important to note that sometimes the catheters are made of a combination of two or more materials mentioned in Table 1 in order to achieve some desired performance characteristics.

[1]The property values of each material in Table 1 only represent the range of its property. Due to different manufacture techniques and procedures, the specific values of the material can vary.

Table 1 Mechanical properties of some materials commonly used for catheters

Materials	Density (kg/m^3)	Young's modulus (MPa)	Poisson's ratio
Polyurethane	1200	25	0.42
Silicone rubber	1100–2300	1–50	0.47–0.49
Teflon/PTFE	2160	400	0.46
Polyethylene	950	700	0.42
Nylon	1100	3000	0.42
Polyvinyl chloride	1400	1500	0.42
Polyimide	1420	2500	0.34
Polyester	1300	3500	0.25
Polyether block amide	1000	12–513	0.34

Table 2 Levels of the factors (density, Young's modulus, and Poisson's ratio) in two factorial design experiments

Trial	Levels	Density (kg/m^3)	Young's modulus (MPa)	Poisson's ratio
First	1	800	50	0.10
	2	1200	300	0.20
	3	1600	1000	0.30
	4	2100	2500	0.40
	5	2500	3500	0.50
Second	1	800	5	0.25
	2	950	20	0.30
	3	1100	40	0.35
	4	1200	60	0.40
	5	1300	80	0.45
	6	1400	100	0.50

Table 3 Specifications of the catheter prototype used in the factorial design experiments

Parameters	Value
Winding turns of axial coil	130
Winding turns of each orthogonal side coil	30
Total length	60 mm
Outer diameter of catheter tubing	3.18 mm
Inner diameter of catheter tubing	1.98 mm
Diameter of axial coil	4.45 mm
Length of axial coil	10 mm
Length of each side coil	10 mm
Width of each side coil	3 mm
Location of center of the coils from catheter tip	15 mm
Diameter of wires	0.064 mm
Density of wires	8940 kg/m^3
Density of blood	1060 kg/m^3
Gravity constant	9.81

Due to the complexity and nonlinearity of the proposed model, the effects of material properties are not straightforward. Therefore, the factorial design experiment approach is used to analyze the effects of the different material properties. Factorial design experiment approach [9] is a systematic method for studying effects of two or more design factors on the response variable, as well as the effects of interactions between factors on the response variable, using a statistical perspective. In this paper, the factors being studied are density, Young's modulus, and Poisson's ratio. The levels of the factors in the experiments are specified in Table 2. Due to unknown relations among these three factors, the first experiment investigates a broad range of the properties[2] which

[2]The combination of the properties may not correspond to one of the existing materials and may require construction of structures combining different materials.

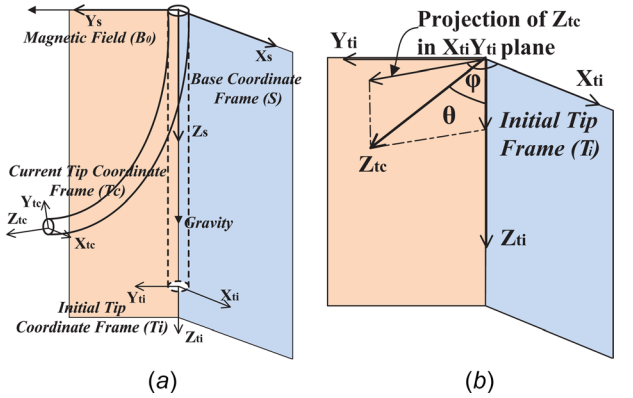

Fig. 4 The definitions of the base and tip coordinate frames. (*a*) The dashed curve represents the initial shape of the catheter under its gravity without actuation. The solid curve represents the shape of the catheter under actuation and gravity. (*b*) The definitions of the deflection angles θ and ϕ. Z_{tc} is the Z unit vector of frame T_c represented in frame T_i.

covers all of the potential materials listed in Table 1. Based on the results from the first experiment, the level selections in the second experiment are refined.

The objective function for evaluating the steering performance is the reachable workspace of the catheter in free space. The specifications of the catheter model embedded with one coil set used in this factorial design experiment are summarized in Table 3. A 3 T homogeneous magnetic field, common in clinical MRI systems, is used. The coils are excited sequentially by a series of currents increasing with a step-size of 50 mA and not exceeding 300 mA. Here, it is assumed that the Joule heating on the coils can be dissipated by employing proper heat management and dissipation strategies.[3] The flexibility of the coil segment is fixed and does not change in the factorial design experiments.

4.2 Computation of Workspace. Figure 4(*a*) shows a catheter deflected in 3D space. The dash and solid curves, respectively, represent the catheter in the zero configuration (when currents are zero) and the deflected catheter with some currents. The base coordinate frame (S) is located on the base of the catheter. The Z axis points along the initial body of the catheter. The tip coordinate frame ($T_{(.)}$) is located on the catheter tip.[4] The Z axis points along the catheter body outward.

In Fig. 4(*a*), the magnetic field vector (B_0) points along the Y_s axis in frame S. The direction of the gravity is along the catheter as this is arguably the worst case deflection configuration, since the catheter would need to lift itself up against the gravity.

As the shape of the workspace in 3D Euclidean space is usually not a regular shape [3], it is difficult to calculate the coverage area by fitting the workspace to any well-known surface. Therefore, the workspace of the catheter is represented by the range of all deflection angles achieved at the catheter tip in polar coordinates relative to the initial catheter direction, as shown in Fig. 4(*b*). The deflection angle θ is the angle between the vector Z_{tc} and the vector Z_{ti} and the deflection angle ϕ is the angle between the projection of the vector Z_{tc} in $X_{ti}Y_{ti}$ plane and the vector X_{ti}. Then these two deflection angles are plotted in a polar coordinate frame where the θ in radians acts as the radius and the ϕ in degree acts

[3]Joule heating that would result in the electromagnetic coils when actuation currents as high as 300 mA are used is an important safety concern, and therefore necessitates application of appropriate heat management and dissipation strategies. Possible heat management and dissipation strategies are discussed in Sec. 7. It is also important to note that the method presented in this paper for kinematic optimization of the catheter design is applicable to any maximum current value.

[4]The subscripts, *ti* and *tc*, for frame (T(.)), respectively, represent the tip frame when it is in the zero configuration and the deflected configuration.

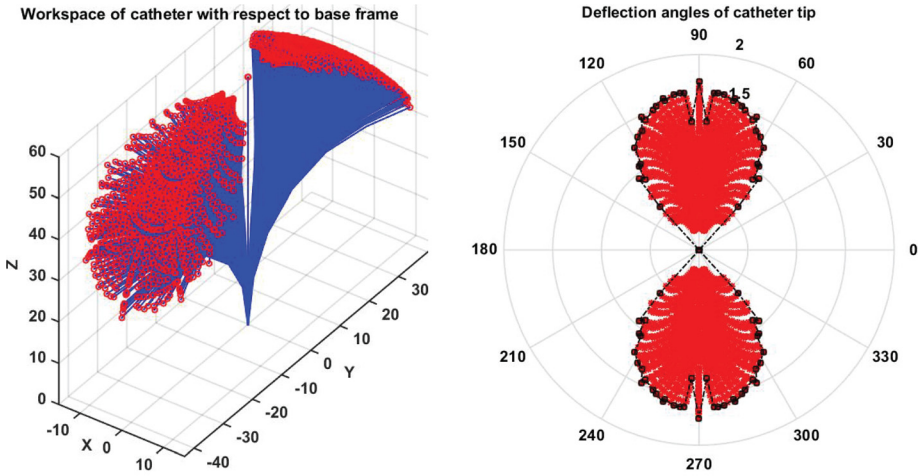

(*a*) (*b*)

Fig. 5 Workspace of a catheter with a single set of actuator coils made of a material with density 800 kg/m^3, Young's modulus 5 MPa, and Poisson's ratio 0.25. (*a*) The workspace in Cartesian space. (*b*) The distribution of the deflection angles in a polar plot.

as the angle (an example is shown in Fig. 5). The area of the resulting closed curve (Fig. 5(*b*)) is used as the quantitative measure of the workspace coverage.

4.3 Results of Material Selection. Figure 6(*a*) shows the main effects of the factors in the first experiment. Young's modulus is the dominant factor affecting the steering performance, particularly in the range of 50–300 MPa. Compared to Young's modulus, the curves for density and Poisson's ratio are much flatter. But the density with smaller values and Poisson's ratio located in the middle range of the selected values can allow the catheter to be more flexible. This experiment narrows down the range of the suitable materials, such as polyurethane, silicone rubber, and polyether block amide. The refined levels of the factors for the second experiment are listed in Table 2.

Figure 6(*b*) shows the main effects of these factors in the second experiment. The results indicate that the lower Young's modulus range of 5–20 MPa resulted in better deflection performance. Among the material types commonly used for catheter construction listed in Table 1, polyurethane, silicone rubber with smaller density and polyether block amide with smaller Young's modulus are the preferable choice from the perspective of the catheter kinematics.

Based on the results of the factorial design analysis, material with Young's modulus of 5 MPa, density of 800 kg/m^3, and Poisson's ratio of 0.25 is chosen. Figure 5(*a*) shows the workspace of the resulting catheter design choice. The blue curves represent the deflected catheter configurations, and the red stars on the tip of the blue curves indicate the catheter tip locations. The 2D workspace represented by deflection angles (in polar coordinates) is shown in Fig. 5(*b*). In this plot, the red stars indicate the deflection angles obtained for different current levels and the black polygon with the dashed lines is the approximate polygon bounding the workspace. The area size of this polygon approximately represents the actual workspace in Cartesian space.

5 Optimization of Actuation

5.1 Description of Left Atrial Ablation Tasks. During the MR-guided ablation procedure, a clinical catheter is inserted into the patient who lies down inside a clinical MRI scanner (Fig. 7(*a*)). In this paper, the ablation task is to create four circular lesions around four ostia of the pulmonary veins on a realistic left atrium model [30] (Fig. 7(*b*)). Atrial fibrillation ablation requires the catheter to be capable of reaching the desired tissue targets and maintaining surface contact with large enough normal contact forces to create sufficiently deep lesions. Therefore, the goal of the actuation optimization is to maximize the deflection coverage and at the same time maximize the normal contact force that the catheter can apply at its tip.

Ho et al. [31] described the anatomic structures of the left atrium. The cavity of the left atrium (Fig. 7(*b*)) is an open space but the internal size is limited. The left atrium model (shown in Fig. 7(*b*)) used in this study for validation has a diameter of approximately 60 mm. Ho et al. [31] also pointed out that the internal wall is relatively smooth. Thus, the friction coefficient between the catheter tip and the internal wall is very low.

How a patient would be positioned inside an MRI scanner [30] and the resulting directions of the gravity and magnetic field vectors relative to the patient[5] are shown in Fig. 7(*a*). Correspondingly, Fig. 7(*b*) shows the relationship between the atrium model and the directions of the magnetic field and the gravity.

5.2 Design Variables

5.2.1 Design Variables of the Electromagnetic Coils. The only actuation source for deflecting the catheter is the magnetic torques from the electromagnetic coils. As we know, a coil set (Fig. 1) can deflect the catheter into an arbitrary direction. Therefore, the structure of the coil set, the number of these sets, Q, and their locations, S, on the catheter have direct impacts on the steering performance.

The torque induced on a current-carrying coil in a magnetic field is given by

$$\boldsymbol{\tau} = \boldsymbol{\mu} \times \mathbf{B} \tag{5}$$

where $\boldsymbol{\tau}$ is the induced torque, $\boldsymbol{\mu}$ is the magnetic moment vector of the coil, and $\mathbf{B}$ is the external magnetic field vector. The magnetic moment vector $\boldsymbol{\mu}$ is

$$\boldsymbol{\mu}_i = N_i \mathbf{A}_i i_i \tag{6}$$

where N_i is the number of winding turns of the ith coil, i_i is the current passing through the ith coil, and $\mathbf{A}_i$ is the vector area of the ith coil (direction of the area vector is given by right-hand rule). The area of the axial coil is determined by its diameter D_a

[5]The global frame is defined by the patient coordinate frame.

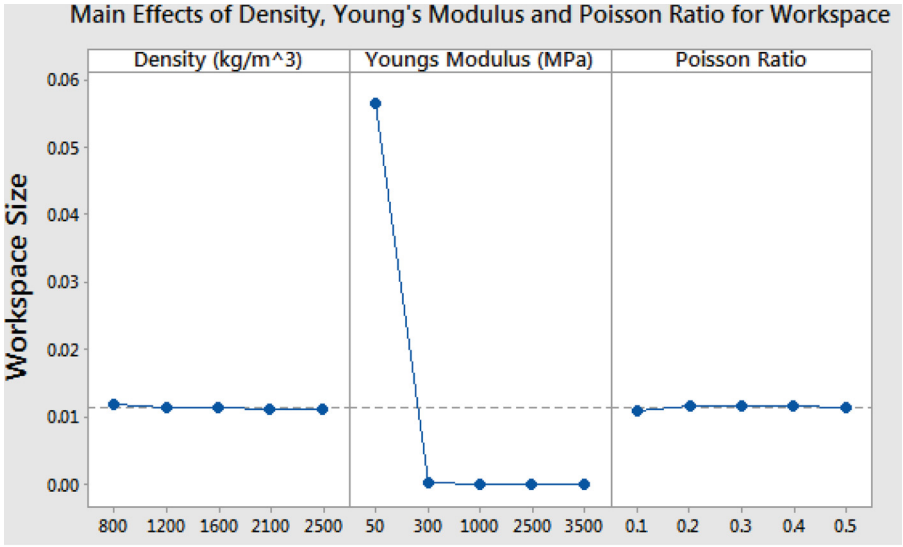

(*a*)

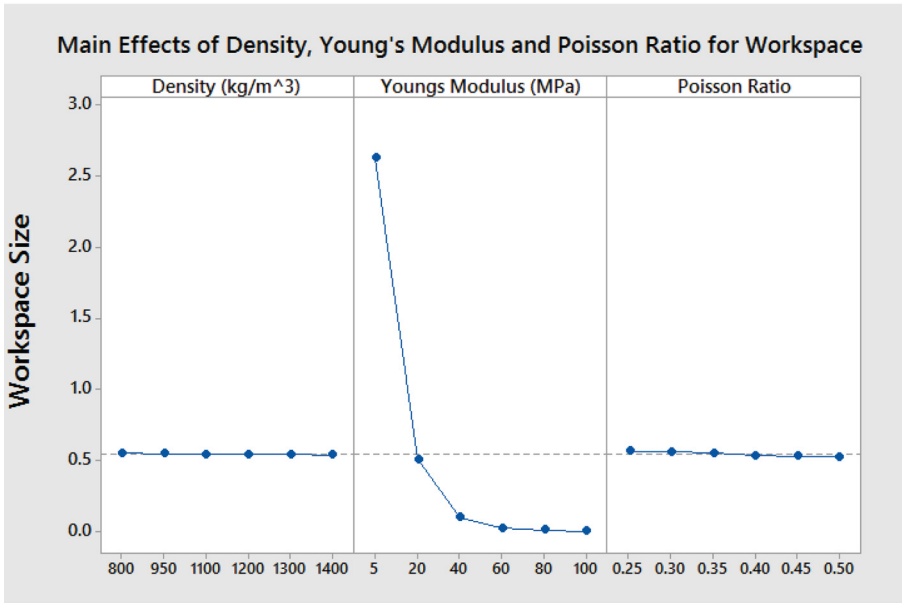

(*b*)

Fig. 6 Results of the factorial design experiments. The units for horizontal axes of density and Young's modulus are kg/m^3 and MPa, respectively. Poisson's ratio and workspace have no unit. (*a*) Main effects plot in the first experiment and (*b*) main effects plot in the second experiment.

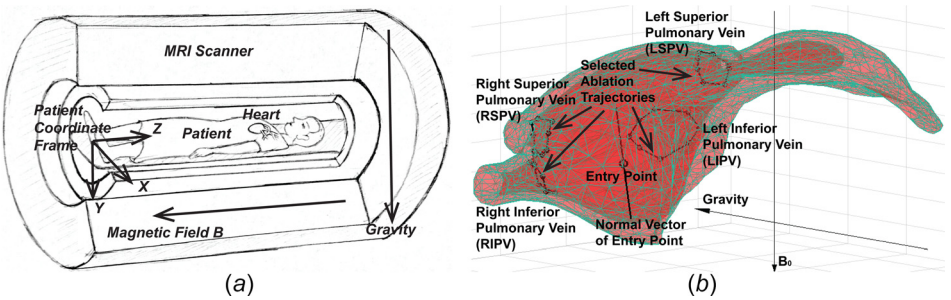

(*a*) (*b*)

Fig. 7 Simulation setup. (*a*) How a patient would be positioned inside an MRI scanner. (*b*) The resulting geometry of the atrial fibrillation ablation task in the left atrium model [30]. The black markers are the desired targets for atrial fibrillation ablation. The black polygons around the pulmonary veins represent the circumferential lesions.

Table 4 Summary of variables and their constraints when there is only one coil set. The unit for distance and length is millimeters.

Variables	Symbols	Constraints
Number of coil sets	Q	$Q = 1$
Winding number of side coil	N_s	$1 \le N_s \le 100$
Winding number of axial coil	N_a	$1 \le N_a \le 300$
Location of coil set away from tip	S_d	$5 \le S_d \le 55$
Length of side coil	L_s	$5 \le L_s \le 50$

and the area of the side coil is determined by its width L_w and length L_s. The diameter of the axial coil D_a and the width of the side coil L_w are constrained to the size of the catheter. Therefore, the length of the side coil L_s and the winding turns N_i of each coil are the design variables in the coil structure. The diameter of the axial coil D_a is set to 5.0 mm and the width of the side coil L_w is set to 3.0 mm.

It is important to note that there is a design trade-off in the choice of coil parameters. Increasing coil size and winding turns increase magnetic torques. On the other hand, they also increase the coil weights, which reduce the performance as the coil actuators have to carry their own weights together with the catheter body during deflection. Furthermore, since coil sets are stiff (approximately ten times or more stiff than the catheter tubing), increasing the size and number of coil sets reduces the flexibility of the catheter. Therefore, it is an additional design trade-off between more actuation power and more flexibility. In order to achieve an appropriate balance among these trade-off factors, a specific and quantitative evaluation of the catheter performance with various levels of these design variables is necessary.

Here, we assume that the two side coils in each coil set have the same geometric structure and share the same number of winding turns for symmetry. Additionally, the length of the side coil is assumed to be equal to the length of the axial coil in each coil set.

5.2.2 Design Variables of Coil Locations. The catheter length limits the number of the coil sets that can be placed on the catheter, and furthermore, constrains the length of the axial coil and the side coils. The total length of the catheter inside left atrium is set to 60 mm.

In this paper, the maximum number of the coil sets, Q, is set to 2. The minimum separation distance between two coil sets is set to 10 mm for allowing a flexural motion. As an electrode is installed to the catheter tip, an appropriate distance between the distal coil set and the tip is necessary to keep. This minimum distance is set to 5 mm in this paper. Additionally, the location of the proximal coil set is also constrained to be away from the base of the catheter. This minimum distance is set to 5 mm in this paper. The maximum winding numbers for axial coil and side coil are determined by the size constraint of the prototype.

In this paper, the optimization problem is divided into two independent problems based on the number of the coil sets. The design variables and their constraints in this problem are summarized in Tables 4 and 5.

5.3 Objective Function. As the magnetic torques of the coils are the only actuation source for deflecting the catheter and providing tip contact force against tissue, maximization of the magnetic torques is the goal of the optimization problem. Increasing contact forces when the catheter is in contact with and constrained by a surface would translate to a corresponding increase in the reachable workspace of the catheter in the absence of the constraint surface. Therefore, similar to the catheter material selection, the actuation coil design parameters are also optimized to maximize the reachable workspace of the catheter in free space. The workspace computation method is explained in Sec. 4.2. The setup of catheter with respect to the magnetic field and gravity is shown in Fig. 4. The maximum current for each coil is set to 300 mA.

Table 5 Summary of variables and their constraints when there are two coil sets. The unit for distance and length is millimeters.

Variables	Symbols	Constraints
Number of coil sets	Q	$Q = 2$
Winding number of side coil	N_{ds}	$1 \le N_{ds} \le 100$
Winding number of axial coil	N_{da}	$1 \le N_{da} \le 300$
Winding number of side coil	N_{ps}	$1 \le N_{ps} \le 100$
Winding number of axial coil	N_{pa}	$1 \le N_{pa} \le 300$
Location of distal coil set away from tip	S_d	$5 \le S_d \le 45$
Length of side coil	L_{ds}	$10 \le L_{ds} \le 20$
Separation distance between two coil sets	Dist.	$10 \le \text{Dist.} \le 45$
Length of side coil	L_{ps}	$10 \le L_{ps} \le 20$
Length constraints		$S_d + L_{ds} + \text{Dist.} + L_{ps} \le 55$

Note: The indices d, p, s, a represent distal coil set, proximal coil set, side coil and axial coil, respectively.

5.4 Results of Coil Design Optimization. The optimization of the coil design parameters was performed using genetic algorithm. The reason is that the mathematical model of the catheter deflection is nonlinear and the optimization problem is nonconvex. Another reason is the large number of design parameters that are being selected and the fact that some of the design parameters are integers (namely, the number of winding turns).

For each of the two subproblems, the genetic algorithm optimization was computed multiple times with different random initial guesses, to alleviate problems with local minima. The results showed that the catheter with two coil sets has much larger workspace than the one with only one coil set. The identified design parameters are summarized in Table 6. Figure 8(*a*) shows the workspace of the resulting catheter design choice in Cartesian space. The stars indicate the catheter tip locations. Similar to Fig. 5(*b*), Fig. 8(*b*) shows the 2D workspace represented by deflection angles and the approximate polygon bounding the workspace. In this plot, the maximum radius representing the θ is 3.14. In other words, the maximum deflection angle is 180 deg, which corresponds to the case where the catheter is actuated to deflect into a U shape. This deflection capability is helpful for performing ablation tasks.

6 Validation Results

In this section, we present a set of simulation studies performed to validate the capability of the catheter prototype recommended by Secs. 4 and 5 to perform atrial fibrillation ablation. Specifically, in the validation studies, the ability of the catheter to perform a realistic atrial fibrillation ablation task (namely, creating circumferential ablation lesions around the right and left pulmonary veins) on a realistic left atrium model [30] (shown in Fig. 7) is evaluated. The catheter is expected to not only follow the

Table 6 Summary of the final design parameters. The unit for distance and length is millimeters.

Variables	N_{ds}	N_{da}	N_{ps}	N_{pa}	S_d	L_{ds}	S_p	L_{ps}
Results	100	300	100	300	5.19	10.15	20.23	12.68

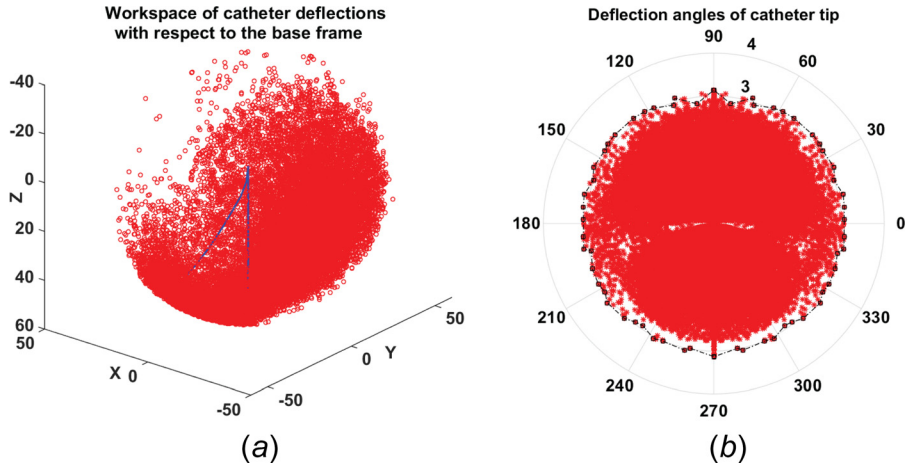

Fig. 8 Workspace of the optimized catheter design. (*a*) The workspace in Cartesian space. The curve shows a deflection motion of catheter. (*b*) The distribution of the deflection angles in a polar plot.

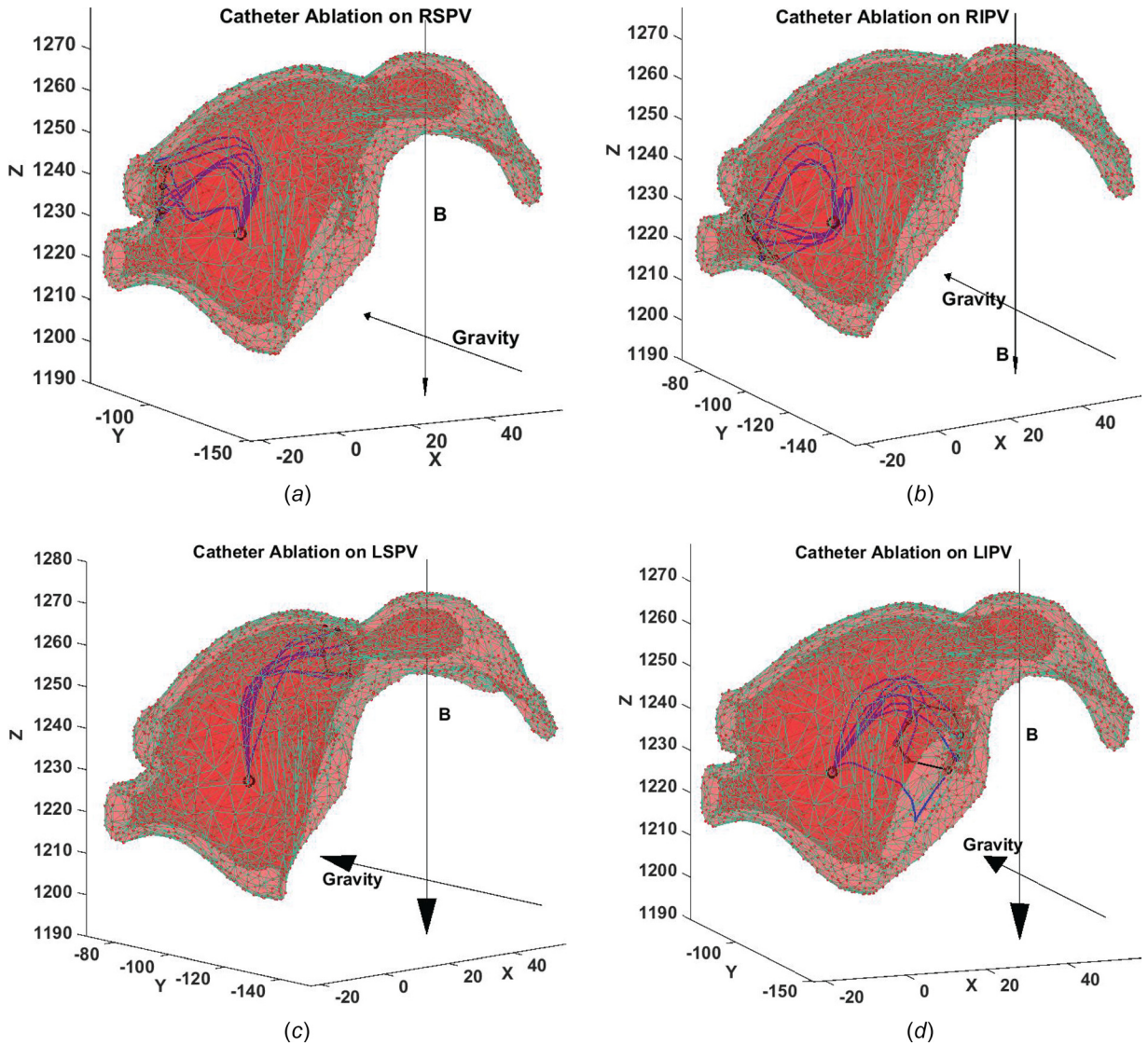

Fig. 9 Computed configurations of the catheter for left atrial fibrillation ablation. Curves represent the deflected catheters. The values marked on the axes denote the coordinates with respect to the patient coordinate frame defined in Fig. 7(*a*). (*a*) Ablation on right superior pulmonary vein (RSPV), (*b*) ablation on right inferior pulmonary vein (RIPV), (*c*) ablation on left superior pulmonary vein (LSPV), and (*d*) ablation on left inferior pulmonary vein (LIPV).

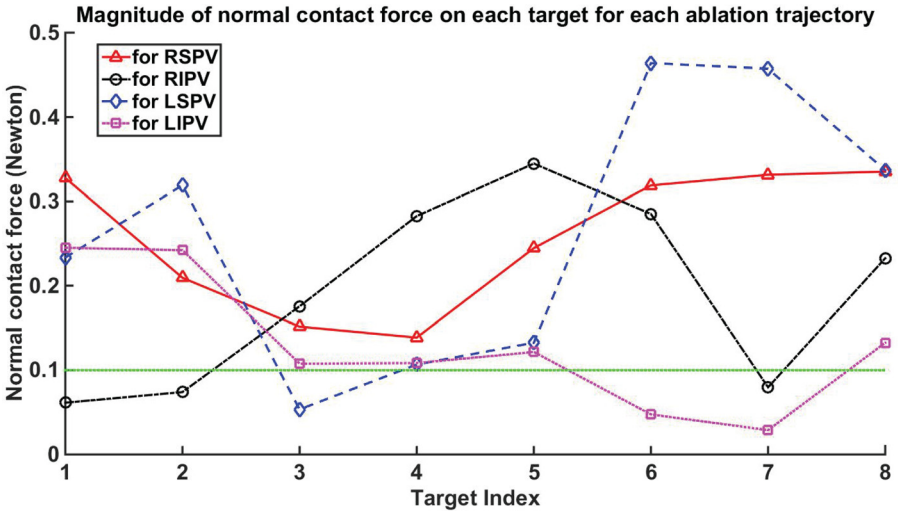

Fig. 10 Magnitude of normal contact force on each ablation target in this simulation

desired ablation trajectory but also push against chamber surface with necessary contact force at the desired ablation locations. In order to guarantee the equilibrium state of the catheter, the static friction force needs to lie inside the friction cone of the contact force.

In this paper, the four circumferential ablation lesions around the pulmonary veins are represented by four sets of eight discrete targets around each of the veins, as shown in Fig. 7(*b*). The task of the catheter, which enters to the left atrium through an entry port on the atrial septum, is to achieve the desired targets and maintain a stable contact by exciting appropriate coils with appropriate currents. To achieve a quasi-stable contact, the catheter needs to be able to generate sufficiently large normal contact forces on the chamber surface, while the tangential component of the contact forces remain within the static friction force cone. Therefore, for each desired point along the trajectory, the simulation maximizes the normal contact force to ensure appropriate contact subject to a list of conditions, represented as

$$\begin{aligned} \underset{i}{\text{maximize}} \quad & |F_{\text{con}}| \\ \text{subject to} \quad & \text{equilibrium equations } (1-2) \\ & F_{\text{fric}} \text{ in friction cone} \\ & |P_{\text{tip}} - P_{\text{target}}| < \text{accuracy} \\ & |F_{\text{con}}| > \text{minimum contact force} \\ & F_{\text{con}} < 0 \end{aligned}$$

where i represents currents for all coils. Additionally, a collision algorithm is implemented during the simulation to ensure that only the tip of the catheter contacts the atrial surface.

In the analysis, a current limit of 300 mA (for each of the coils), a minimum normal contact force of 10 g (100 mN), a target accuracy of 1 mm, and a static friction coefficient of 0.2 were used. Also, a 3 T homogeneous magnetic field was used in the analysis.

All configurations of the catheter for ablation on left superior pulmonary vein (LSPV), left inferior pulmonary vein (LIPV), right superior pulmonary vein (RSPV), and right inferior pulmonary vein (RIPV) are computed, as shown in Fig. 9. The curves represent the deflected catheter in the left atrium. The markers are the desired targets around pulmonary veins.

For each circle enclosing one of the ostium of the pulmonary veins, one insertion length of the catheter is preferred as the insertion motion will potentially change the relationship between the direction of the coil and the direction of magnetic field, which will play a significant effect on the deflection motion when the coils are actuated. Constant insertion lengths of 50 mm, 49 mm, 57 mm, and 55 mm were used for RSPV, RIPV, LSPV, and LIPV, respectively.

The validation results confirm that the proposed catheter design is able to successfully reach all of the desired target locations within a 1 mm position error. The magnitudes of the normal contact forces on each target in this simulation are shown in Fig. 10. The catheter is able to generate the desired normal contact forces for all of the RSPV targets and most of the other targets. However, the normal contact forces for two RIPV targets (the first and second targets), one LSPV target (the third target), and two LIPV targets (the sixth and seventh targets) are below the targeted 10 g (100 mN), but are still well above 1 g (10 mN).

Figure 11 shows the workspace of the catheter prototype with an insertion length, 60 mm. The circles represent the tip locations of the catheter. The coverage of the workspace is able to reach the ostia of the pulmonary veins. One possible approach to improve access of the catheter to different targets is to change the orientation of the catheter base with respect to the entry port (the normal vector shown in Fig. 11) on the atrial septum by using a guide wire.

The steering performance of the catheter depends on the generated torques from the interaction of current-carrying electromagnetic coils and the B_0 field of the scanner. During the procedure, the lying pose of the patient and the structure of the patient's heart

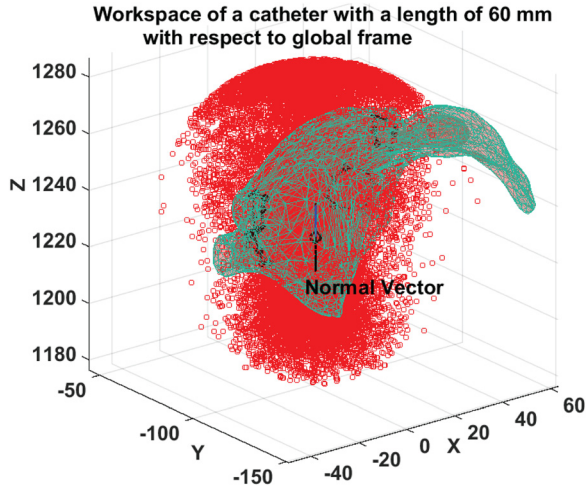

Fig. 11 Workspace of a catheter prototype with an insertion length, 60 mm, with respect to the global frame

(shown in Fig. 7(*a*)) determine the direction relationships between the B_0 field and the surface of atrium septum to a great extent, although the surface of atrium septum is not a definite plane. The catheter's entry point on the transceptal wall will play an important role on the steering performance and force capability of the catheter. Jayender et al. [32] investigated the relationship of the performances of the catheter with respect to different entry points on the atrial septum, although their catheter is a cable-driven catheter whose actuation is not related to any magnetic field. Entry point selection for an MRI-actuated steerable catheter system could be investigated as part of future work.

7 Conclusions

This paper proposed a systematic approach to the design optimization of an MRI-actuated steerable catheter for atrial fibrillation ablation in the left atrium. First, factorial design experiments were conducted to investigate the relationship between the catheter material and the catheter's steering performance. Specifically, the effects of the mechanical properties of the material, such as, Young's modulus, density, and Poisson's ratio, were investigated. It was found out that Young's modulus is the most important parameter for the steering performance of the catheter. Following the material selection, the design optimization of the electromagnetic coils was performed to select the optimal winding turns for the coils, the optimal size for the side coils, and the optimal locations of the coil sets on the catheter. Finally, the selected catheter design was validated on a simulated atrial fibrillation ablation in a realistic left atrium model. The simulation verified that the catheter was successfully able to reach every target on the circumferential lesions. Additionally, the achievable contact force between the catheter tip and the chamber was also investigated. For most of the targets, the catheter can provide at least a 10 g force (100 mN).

There is a trade-off between the coil sizes and the catheter deflection. Specifically, since the coil sets are much stiffer than the catheter body (approximately 10× or more stiff), increasing the size and number of coil sets reduces the flexibility of the catheter while it increases the generated magnetic torques.

It is important to note that the Joule heating in the electromagnetic coils is an important safety concern in the proposed actuation scheme. Specifically, the maximum current value of 300 mA used in the catheter design optimization, when applied to a 300-turn 42-gauge wire microcoil, would potentially results in substantial Joule heating (and hence unsafe temperature increases) in the coils without implementing any active cooling of the catheter or a heat management strategy. This problem has not been explicitly considered in this study, as the heat generation and dissipation characteristics are intimately dependent on the specifics of the physical construction of the catheter. There are multiple approaches that can be employed for management of the generated heat, to prevent the heat from dissipating outward to the surrounding blood and chamber cavity and to safely dissipate the generated heat. Some possible approaches include adding a layer of thermal insulation coating on the coils to keep the heat inside, winding coils on a lightweight heat conductor, e.g., aluminum oxide substrate, and passing saline coolant through catheter lumen to actively cool the heating coils (e.g., as proposed in Ref. [33]). This heat management problem is addressable and deserves further study in the future.

Acknowledgment

This work was supported in part by National Science Foundation under Grant Nos. CISE IIS-1524363 and IIS-1563805, and National Institutes of Health under Grant No. R01 EB018108.

References

[1] Chowdhury, P., Lewis, W. R., Schweikert, R. A., and Cummings, J. E., 2009, "Ablation of Atrial Fibrillation: What Can We Tell Our Patients?," Cleveland Clin. J. Med., **76**(9), pp. 543–550.

[2] Dewire, J., and Calkins, H., 2010, "State-of-the-Art and Emerging Technologies for Atrial Fibrillation Ablation," Nat. Rev. Cardiol., **7**(3), pp. 129–138.

[3] Nazarian, S., Kolandaivelu, A., Zviman, M. M., Meininger, G. R., Kato, R., Susil, R. C., Roguin, A., Dickfeld, T. L., Ashikaga, H., Calkins, H., Berger, R. D., Bluemke, D. A., Lardo, A. C., and Halperin, H. R., 2008, "Feasibility of Real-Time Magnetic Resonance Imaging for Catheter Guidance in Electrophysiology Studies," Circulation, **118**(3), pp. 223–229.

[4] Vergara, G. R., Vijayakumar, S., Kholmovski, E. G., Blauer, J. J. E., Guttman, M. A., Gloschat, C., Payne, G., Vij, K., Akoum, N. W., Daccarett, M., McGann, C. J., MacLeod, R. S., and Marrouche, N. F., 2011, "Real-Time Magnetic Resonance Imaging-Guided Radiofrequency Atrial Ablation and Visualization of Lesion Formation at 3 Tesla," Heart Rhythm, **8**(2), pp. 295–303.

[5] Roberts, T. P. L., Hassenzahl, W. V., Hetts, S. W., and Arenson, R. L., 2002, "Remote Control of Catheter Tip Deflection: An Opportunity for Interventional MRI," Magn. Reson. Med., **48**(6), pp. 1091–1095.

[6] Gudino, N., Heilman, J. A., Derakhshan, J. J., Sunshine, J. L., Duerk, J. L., and Griswold, M. A., 2011, "Control of Intravascular Catheters Using an Array of Active Steering Coils," Med. Phys., **38**(7), pp. 4215–4224.

[7] Liu, T., and Cavusoglu, M. C., 2014, "Three Dimensional Modeling of an MRI Actuated Steerable Catheter System," International Conference on Robotics and Automation (ICRA), Hong Kong, China, May 31–June 7, pp. 4393–4398.

[8] Liu, T., Poirot, N. L., Franson, D., Seiberlich, N., Griswold, M. A., and Cavusoglu, M. C., 2016, "Modeling and Validation of the Three-Dimensional Deflection of an MRI-Compatible Magnetically Actuated Steerable Catheter," IEEE Trans. Biomed. Eng., **63**(10), pp. 2142–2154.

[9] Montgomery, D. C., 2009, *Design and Analysis of Experiments*, Wiley, Hoboken, NJ.

[10] Fu, Y., Liu, H., Huang, W., Wang, S., and Liang, Z., 2009, "Steerable Catheters in Minimally Invasive Vascular Surgery," Int. J. Med. Rob. Comput., **5**(4), pp. 381–391.

[11] Muller, L., Saeed, M., Wilson, M., and Hetts, S., 2012, "Remote Control Catheter Navigation: Options for Guidance Under MRI," J. Cardiovasc. Magn. Reson., **14**(1), p. 33.

[12] Hetts, S. W., Saeed, M., Martin, A., Lillaney, P., Losey, A., Yee, E. J., Sincic, R., Do, L., Evans, L., Malba, V., Bernhardt, A. F., Wilson, M. W., Patel, A., Arenson, R. L., Caton, C., and Cooke, D. L., 2013, "Magnetically-Assisted Remote Controlled Microcatheter Tip Deflection Under Magnetic Resonance Imaging," J. Visualized Exp., **74**, p. 50299.

[13] Settecase, F., Sussman, M. S., Wilson, M., Hetts, S., Arenson, R., Malba, V., Bernhardt, A., and Roberts, T. P. L., 2007, "Magnetically-Assisted Remote Control (MARC) Steering of Endovascular Catheters for Interventional MRI: An Equation for Predicting Deflection and Experimental Validation," Med. Phys., **34**(8), pp. 3135–3142.

[14] Losey, A. D., Lillaney, P., Martin, A. J., Cooke, D. L., Wilson, M. W., Thorne, B. R. H., Sincic, R. S., Arenson, R. L., Saeed, M., and Hetts, S. W., 2014, "Magnetically Assisted Remote-Controlled Endovascular Catheter for Interventional MR Imaging: In Vitro Navigation at 1.5 T Versus X-Ray Fluoroscopy," Radiology, **271**(3), pp. 862–869.

[15] Moftakhar, P., Lillaney, P., Losey, A. D., Cooke, D. L., Martin, A. J., Thorne, B. R. H., Arenson, R. L., Saeed, M., Wilson, M. W., and Hetts, S. W., 2015, "New-Generation Laser-Lithographed Dual-Axis Magnetically Assisted Remote-Controlled Endovascular Catheter for Interventional MR Imaging: In Vitro Multiplanar Navigation at 1.5 T and 3 T Versus X-Ray Fluoroscopy," Radiology, **277**(3), pp. 842–852.

[16] Lalande, V., Gosselin, F. P., and Martel, S., 2010, "Catheter Steering Using a Magnetic Resonance Imaging System," Annual International Conference of the IEEE Engineering in Medicine and Biology (EMBC), Buenos Aires, Argentina, Aug. 31–Sept. 4, pp. 1874–1877.

[17] Gosselin, F. P., Lalande, V., and Martel, S., 2011, "Characterization of the Deflections of a Catheter Steered Using a Magnetic Resonance Imaging System," Med. Phys., **38**(9), pp. 4994–5002.

[18] Magnetecs, 2017, "Catheter Guidance Control and Imaging (CGCI) System," Magnetecs Corp., Inglewood, CA, accessed Jan. 16, 2017, http://www.magnetecs.com/overview.php

[19] Stereotaxis, 2016, "Niobe® ES Magnetic Navigation System," Stereotaxis, Inc., St. Louis, MO, accessed Jan. 16, 2017, http://www.stereotaxis.com/products/niobe/

[20] Ullrich, F., Schuerle, S., Pieters, R., Dishy, A., Michels, S., and Nelson, B. J., 2014, "Automated Capsulorhexis Based on a Hybrid Magnetic-Mechanical Actuation System," IEEE International Conference on Robotics and Automation, (ICRA), Hong Kong, China, May 31–June 7, pp. 4387–4392.

[21] Di Biase, L., Natale, A., Barrett, C., Tan, C., Elayi, C. S., Ching, C. K., Wang, P., Al-Ahmad, A., Arruda, M., Burkhardt, J. D., Wisnoskey, B. J., Chowdhury, P., De Marco, S., Armaganijan, L., Litwak, K. N., Schweikert, R. A., and Cummings, J. E., 2009, "Relationship Between Catheter Forces, Lesion Characteristics, "Popping," and Char Formation: Experience With Robotic Navigation System," J. Cardiovasc. Electrophysiol., **20**(4), pp. 436–440.

[22] Makimoto, H., Lin, T., Rillig, A., Metzner, A., Wohlmuth, P., Arya, A., Antz, M., Mathew, S., Deiss, S., Wissner, E., Rausch, P., Bardyszewski, A., Kamioka, M., Li, X., Kuck, K.-H., Ouyang, F., and Tilz, R. R., 2014, "In Vivo Contact Force Analysis and Correlation With Tissue Impedance During Left Atrial Mapping and Catheter Ablation of Atrial Fibrillation," Circ. Arrhythmia Electrophysiol., **7**(1), pp. 46–54.

[23] Bergeles, C., Gosline, A., Vasilyev, N., Codd, P., del Nido, P., and Dupont, P., 2015, "Concentric Tube Robot Design and Optimization Based on Task and Anatomical Constraints," IEEE Trans. Rob., **31**(1), pp. 67–84.

[24] Torres, L., Webster, R., and Alterovitz, R., 2012, "Task-Oriented Design of Concentric Tube Robots Using Mechanics-Based Models," IEEE/RSJ International Conference on Intelligent Robots and Systems (IROS 2012), Vilamoura-Algarve, Portugal, Oct. 7–12, pp. 4449–4455.
[25] Burgner, J., Gilbert, H., and Webster, R., 2013, "On the Computational Design of Concentric Tube Robots: Incorporating Volume-Based Objectives," IEEE International Conference on Robotics and Automation (ICRA), Karlsruhe, Germany, May 6–10, pp. 1193–1198.
[26] Liu, T., 2017, "A Magnetically-Actuated Robotic Catheter for Atrial Fibrillation Ablation Under Real-Time Magnetic Resonance Imaging Guidance," Ph.D. thesis, Case Western Reserve University, Cleveland, OH.
[27] Werneth, R., Sherman, M., Castellano, T., Flaherty, J., and Currie, G., 2013, "Ablation Catheter," U.S. Patent No. 8486063.
[28] Nguyen, F., 2003, "Steerable Catheter With a Control Handle Having a Pulley Mechanism," U.S. Patent No. 6,522,933.
[29] Kunis, C., Castellano, T., Sherman, M., and Werneth, R., 2012, "Atrial Ablation Catheter and Method of Use," U.S. Patent No. 8,273,084.
[30] Mitsuhashi, N., Fujieda, K., Tamura, T., Kawamoto, S., Takagi, T., and Okubo, K., 2009, "BodyParts3D: 3D Structure Database for Anatomical Concepts," Nucleic Acids Res., **37**(Suppl. 1), pp. D782–D785.
[31] Ho, S. Y., Cabrera, J. A., and Sanchez-Quintana, D., 2012, "Left Atrial Anatomy Revisited," Circ. Arrhythmia Electrophysiol., **5**(1), pp. 220–228.
[32] Jayender, J., Patel, R., Michaud, G., and Hata, N., 2011, "Optimal Transseptal Puncture Location for Robot Assisted Left Atrial Catheter Ablation," Int. J. Med. Rob., **7**(2), pp. 193–201.
[33] Hetts, S., Saeed, M., Martin, A., Evans, L., Bernhardt, A., Malba, V., Settecase, F., Do, L., Yee, E., Losey, A., Sincic, R., Lillaney, P., Roy, S., Arenson, R., and Wilson, M., 2013, "Endovascular Catheter for Magnetic Navigation Under MR Imaging Guidance: Evaluation of Safety In Vivo at 1.5T," Am. J. Neuroradiol., **34**(11), pp. 2083–2091.